

DUST ATTENUATION OF THE NEBULAR REGIONS OF $z \sim 2$ STAR-FORMING GALAXIES: INSIGHT FROM UV, IR, AND EMISSION LINESS. DE BARROS^{1,2,3}, N. REDDY^{1,4}, I. SHIVAEI^{1,5}

ABSTRACT

We use a sample of 149 spectroscopically confirmed UV-selected galaxies at $z \sim 2$ to investigate the relative dust attenuation of the stellar continuum and the nebular emission lines. For each galaxy in the sample, at least one rest-frame optical emission line ($H\alpha/[N\text{ II}] \lambda 6583$ or $[O\text{ III}] \lambda 5007$) measurement has been taken from the literature, and 41 galaxies have additional *Spitzer*/*MIPS* 24 μm observations that are used to infer infrared luminosities. We use a spectral energy distribution (SED) fitting code that predicts nebular line strengths when fitting the stellar populations of galaxies in our sample, and we perform comparisons between the predictions of our models and the observed/derived physical quantities. We find that on average our code is able to reproduce all the physical quantities (e.g., UV β slopes, infrared luminosities, emission line fluxes), but we need to apply a higher dust correction to the nebular emission compared to the stellar emission for the largest SFR ($\log(\text{SFR}/M_{\odot}\text{yr}^{-1}) > 1.82$, Salpeter IMF). We find a correlation between SFR and the difference in nebular and stellar color excesses, which could resolve the discrepant results regarding nebular dust correction at $z \sim 2$ from previous results.

Subject headings: dust, extinction — galaxies: starburst — galaxies: evolution — galaxies: high-redshift

1. INTRODUCTION

Nebular emission (i.e. lines and nebular continuum from H II regions) is ubiquitous in regions of massive star-formation, strong or dominant in the optical spectra of nearby star-forming galaxies, and present in numerous types of galaxies. While several spectral models of galaxies including nebular emission exist (e.g., Charlot & Longhetti 2001; Fioc & Rocca-Volmerange 1997; Anders & Fritze-v. Alvensleben 2003; Zackrisson et al. 2008), the impact of nebular emission on the determination of physical parameters of galaxies, in particular at high redshift, has been largely neglected until recently. Zackrisson et al. (2008) showed that nebular emission can significantly affect broadband photometry; the impact becoming stronger with increasing redshift, as the equivalent width (EW) of emission lines scales with $(1+z)$. The nebular emission contribution to broad-band photometry at high redshift can lead to overestimates of stellar masses (M_{\star}) and ages (e.g., Schaerer & de Barros 2009; Ono et al. 2010; Schaerer & de Barros 2010).

Until recently, the derived evolution of the specific star-formation rate (sSFR=star-formation rate/ M_{\star}) with redshift, which indicated an sSFR “plateau” at $z > 2$ (e.g., Stark et al. 2010; González et al. 2010), was in conflict with the expected sSFR- z evolution inferred from hydrodynamical simulations (e.g., Bouché et al. 2010; Davé et al. 2011), which suggest that the sSFR should increase with redshift. Accounting for nebular emission can possibly reconcile the observations with theoretical expectations of the sSFR evolution (Stark et al. 2013; de Barros et al. 2014; Duncan et al. 2014; Salmon et al. 2015). More generally, an accurate and physically motivated modeling of nebular emission is necessary

to obtain more precise constraints on the physical properties of high-redshift galaxies, the cosmic star-formation history (Salmon et al. 2015), and reionization (Robertson et al. 2010).

While NIR multi-object spectrographs like MOSFIRE (McLean et al. 2012) have enabled measurements of a number of rest-optical emission lines (e.g., $H\beta$, $H\alpha$, $[O\text{ III}]$) up to $z \sim 3.7$ (Holden et al. 2014; Kriek et al. 2015), these lines remain inaccessible at $z > 3.7$, at least until the launch of the *James Webb Space Telescope*. However, it is possible to find empirical evidence of strong emission lines at $z > 3.7$ by observing a flux increase in a band which cannot be explained with pure stellar emission and where a strong emission line is expected (e.g., Chary et al. 2005; Shim et al. 2011; Stark et al. 2013; de Barros et al. 2014; Smit et al. 2014). Uncertainties remain relatively large because the inferred strength of the lines depends on constraints on the stellar continuum and hence on other inferred galaxy properties (e.g., age, dust extinction). One way to avoid this issue is to model both stellar and nebular emission simultaneously (e.g., Schaerer & de Barros 2009, 2010). This method must rely on several assumptions such as the Lyman continuum escape fraction, the metallicity, and the density and temperature of the ionized gas. These parameters remain largely unconstrained at $z > 3.7$, although there is mounting evidence that ISM physical conditions evolve with redshift (Kewley et al. 2013b; Nakajima & Ouchi 2014; Steidel et al. 2014; Shapley et al. 2015).

Until now, most studies on the impact of nebular emission on galaxy physical properties at $z > 3.7$ have assumed that both nebular and stellar emission suffer the same amount of dust attenuation (e.g., Ono et al. 2012; Robertson et al. 2010, 2013; Vanzella et al. 2010, 2014; Labbé et al. 2010, 2013; Oesch et al. 2013a,b, 2014; de Barros et al. 2014; Duncan et al. 2014; Salmon et al. 2015; Smit et al. 2014). However, evidence for an excess of nebular color excess relative to the stellar color excess in local starburst galaxies has been provided through the comparison of optical depths between Balmer lines ($H\alpha$ and $H\beta$) and the stellar continuum

¹ Department of Physics and Astronomy, University of California, Riverside, CA 92507

² INAF-Bologna Astronomical Observatory, via Ranzani 1, I-40127 Bologna, Italy, email: stephane.debarros@oabo.inaf.it

³ Swiss National Science Foundation Fellow

⁴ Alfred P. Sloan Research Fellow

⁵ NSF Graduate Research Fellow

(Calzetti et al. 1994, 1997, 2000). This difference in color excess can be explained by the fact that star-formation occurs in regions of high gas and dust column density. UV and optical stellar continuum are produced by ionizing and non-ionizing stars. On the other hand, the nebular emission arises around regions of short-lived massive stars which may not leave their dusty birthplaces, while less massive stars can diffuse into less dusty regions. This could partly explain why nebular emission shows a higher color excess than the stellar continuum emission for local star-forming galaxies (Calzetti et al. 1997). The analysis presented in Wild et al. (2011) also shows that the nebular to stellar attenuation is related to the sSFR and axial ratio.

Measuring the relative color excess of the stellar continuum and nebular lines at high redshift has been difficult until recently (Reddy et al. 2015) due to the lack of measurements of both $H\alpha$ and $H\beta$ lines for large galaxy samples. One way to compare the stellar and nebular color excess is to derive the dust extinction of the stellar continuum through SED fitting and then compare dust corrected SFRs inferred from emission lines (e.g., $H\alpha$) with another dust-corrected SFR indicator. Under the assumption of a constant star-formation history for ~ 100 Myr, $SFR(UV)$ and $SFR(H\alpha)$ should equilibrate to the same value (Kennicutt 1998) and any remaining discrepancy between these two SFR tracers may be due to a different dust extinction between the regions of nebular emission and the stellar continuum, although there are other possibilities (e.g., initial mass function variations). The possible effect of the star-formation history must be taken into account when using $SFR(H\alpha)/SFR(UV)$ to infer whether there is a difference in the color excess of the stellar continuum and nebular regions. While this kind of comparison has been used extensively at high redshift (e.g., Erb et al. 2006a; Förster Schreiber et al. 2009; Reddy et al. 2010; Mancini et al. 2011; Holden et al. 2014; Shivaei et al. 2015), the existence of higher nebular color excess relative to stellar color excess remains unclear: Erb et al. (2006a) and Reddy et al. (2010) find that assuming a similar color excess between the stellar continuum and nebular regions results in the best agreement between UV and $H\alpha$ -based SFRs, while several other studies find that extra extinction is required (Kashino et al. 2013; Price et al. 2014). A possible explanation for these discrepant results found at $z \sim 2$ is that the trend between the nebular versus stellar color excesses depends on SFR, as was suggested in Reddy et al. (2010) and Yoshikawa et al. (2010), or the nebular to stellar attenuation can also depend on the sSFR (Wild et al. 2011; Price et al. 2014).

Direct measurements of the Balmer decrement ($H\alpha/H\beta$ flux ratio) have been lacking for high-redshift galaxies, until recently, and these observations have been possible because of recent new instruments as the Wide-Field-Camera 3 of the *Hubble Space Telescope*, the Fiber Multi Object Spectrograph on the Subaru Telescope (Kimura et al. 2010), and the Multi-Object Spectrometer for Infra-Red Exploration on the Keck Telescope (McLean et al. 1998). At $z \sim 1.5$, Domínguez et al. (2013), Kashino et al. (2013) and Price et al. (2014) provide Balmer decrement measurements for relatively large samples of galaxies, but via stacking as the $H\beta$ line is typically undetected for individual galaxies. Kashino et al. (2013) find a higher nebular color excess relative to stellar color excess, but the ratio between the two is lower than the one found for local star-forming galaxies (Calzetti et al. 2000). The results from Price et al. (2014), based on stacked data, are consistent with a difference in color excess between nebular and

stellar emission, but they also examine possible correlations between color excess ratio and the other physical parameters (M_* , SFR, sSFR). Interestingly, they find that the difference in the color excess between nebular and stellar emission increases with decreasing sSFR (Price et al. 2014, Figure 4). They interpret this correlation with a two-component dust model, whereby H II regions are dustier than the diffuse ISM outside stellar birth clouds. The continuum light coming from galaxies with high sSFR would be almost completely dominated by emission from H II regions, while the emitted rest-optical continuum from low sSFR galaxies would be dominated by less massive stars located outside H II regions. Therefore, for high sSFR galaxies, both nebular and stellar emission would be equally attenuated and for low sSFR galaxies, nebular emission would be more attenuated than stellar continuum (Price et al. 2014, Figure 5). An opposite trend is found in Reddy et al. (2015) with the nebular to stellar color excess ratio increasing with increasing sSFR, using the largest sample including individual Balmer decrement measurements at these redshifts.

We build upon these previous studies by using the approach described in Schaerer et al. (2013), which has been already used to analyze a small sample of lensed galaxies in Sklias et al. (2014). Namely, we derive the properties of a large number of individual galaxies by comparing several observables (broad-band photometry, emission line fluxes, infrared luminosities) with predictions from stellar population synthesis models that include nebular emission. We consider a range of star-formation histories in the SED-fitting in order to minimize the number of assumptions going into our analysis. This study has several aims: the first is to test the ability of our SED fitting method to reproduce observed quantities, particularly emission line fluxes. Once our SED fitting code is tuned to reproduce the observables, we determine and compare correlations among physical properties of individual galaxies. Our approach is complementary to the one used in Reddy et al. (2015), because we are using SED-fitting code to examine these issues.

The paper is structured as follows. The selection procedure, spectroscopic and photometric data, and the final sample used in this work are described in Sect. 2. The method used to derive physical parameters and to model the nebular emission is described in Sect. 3. The ability of our method to reproduce emission line fluxes is described in Sect. 4 and the implications regarding the dust extinction toward nebular regions are discussed in Sect. 5. Section 6 summarizes our main conclusions. We adopt a Λ -CDM cosmological model with $H_0 = 70$ km s $^{-1}$ Mpc $^{-1}$, $\Omega_m = 0.3$ and $\Omega_\Lambda = 0.7$. We assume a Salpeter IMF (Salpeter 1955). All magnitudes are expressed in the AB system (Oke & Gunn 1983).

2. DATA

2.1. Selection, optical and near-IR data

All the data used in this paper are taken from the literature. In the following, we provide only brief descriptions of the data acquisition and reduction. The reader is invited to consult the references given below for more details.

We start with a large UV-selected galaxy sample, with photometric and spectroscopic observations described in Steidel et al. (2003), Steidel et al. (2004), and Adelberger et al. (2004). The selection is based on U_nGR colors. All the galaxies in our sample are spectroscopically confirmed with rest-frame UV observations conducted with

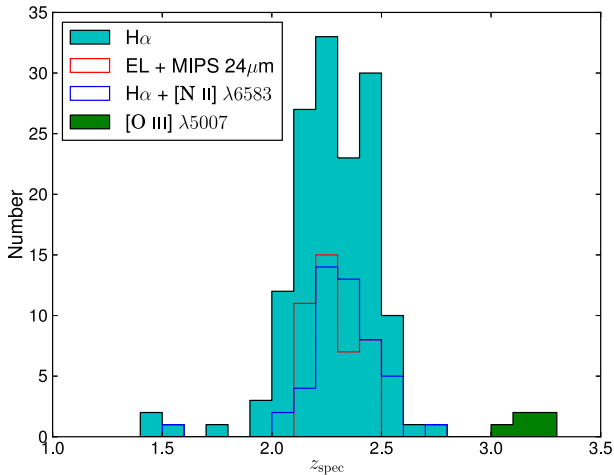


Figure 1. Redshift distribution of the star-forming galaxy sample. All galaxies have $H\alpha$ measurements (Erb et al. 2006a; Kulas et al. 2012, 2013), except 5 galaxies at $z > 3$ for which we have $[O\ III]\ \lambda 5007$ measurements (Kulas et al. 2012). $[N\ II]\ \lambda 6583$ measurements are taken from Kulas et al. (2013).

the Keck/LRIS spectrograph (Oke et al. 1995).

Photometry in the J and K_S band are obtained with the Palomar/WIRC and Magellan/PANIC instruments (Shapley et al. 2005). These data provide important constraints on the Balmer break, which can be used to estimate the age of the stellar population.

Our photometry includes *Hubble*/WFC3 F160W observations (Law et al. 2012) which provide more robust constraints on the Balmer and 4000 Å breaks. We combine ground-based U_rGR optical photometry with J , K_S , and F160W data with *Spitzer*/IRAC observations in the four available channels ($3.6\mu\text{m}$, $4.5\mu\text{m}$, $5.8\mu\text{m}$, and $8.0\mu\text{m}$). Details regarding the fields of view and photometry can be found in Reddy et al. (2006a) and Reddy et al. (2012b). The latter reference provides a complete description of the data used in our study.

To more robustly constrain the physical parameters of galaxies studied in this paper, we add available near-infrared spectroscopic data taken with the NIRSPEC instrument (McLean et al. 1998) presented in Erb et al. (2006b). These observations provide $H\alpha$ flux measurements for 91 of our galaxies. Additional NIRSPEC spectroscopy is taken from Kulas et al. (2012), which provides $H\alpha$ and $[O\ III]\ \lambda 5007$ flux measurements for 5 and 5 galaxies respectively. We also use spectroscopic observations (Kulas et al. 2013) performed with the recently commissioned Keck/MOSFIRE near-infrared spectrometer (McLean et al. 2012). This allows us to add 48 measurements of both $H\alpha$ and $[N\ II]\ \lambda 6583$ fluxes to our study. The main source of flux measurement uncertainties for both NIRSPEC and MOSFIRE instruments come from slit losses and are estimated to be close to ~ 2 (Erb et al. 2006a; Steidel et al. 2014). This average slit loss is mainly due to seeing conditions and not to the size of galaxies: for the stellar mass range probed here, at $z \sim 2$, half-light radius is typically $0''.2 - 0''.3$ (Price et al. 2015), well within the NIRSPEC and MOSFIRE slits used to obtain the data (Erb et al. 2006b; Kulas et al. 2012, 2013). Therefore we correct the observed fluxes by a factor 2. The Erb et al. (2006b) and Kulas et al. (2012) samples probe similar range of stellar masses and SFRs as stated in this latter reference. The galaxies from the Kulas et al. (2013) sample are more massive on average ($10^{10}M_\odot \lesssim M_\star \lesssim 10^{11}M_\odot$) but still in the stellar mass

range probed in Erb et al. (2006b) and Kulas et al. (2012).

Finally, combining photometric and spectroscopic data described in this section, we obtain a sample of 149 galaxies with extensive broad-band photometric coverage, and $H\alpha$ and $[O\ III]\ \lambda 5007$ flux measurements for 144 and 5 galaxies respectively. $[N\ II]\ \lambda 6583$ measurements exist for a subsample of 48 galaxies with $H\alpha$ observations.

2.2. Mid-IR data

MIPS $24\mu\text{m}$ data in the GOODS-North field and four LBG fields (Q1549, Q1623, Q1700, and Q2343; Reddy & Steidel 2009) are used to measure the rest-frame $8\mu\text{m}$ fluxes of galaxies at $z \sim 2$. The complete photometry and extraction method is described in Reddy et al. (2010). The measured $8\mu\text{m}$ luminosities are then converted to the total IR luminosity (i.e., IR luminosity integrated over 8-1000 μm) using Chary & Elbaz (2001) templates, and are corrected for the luminosity dependence of the conversion, as derived from stacked *Herschel* data for a similarly-selected sample of galaxies (Reddy et al. 2012a). This latter reference compared L(IR) computed from 24, 100, 160 μm , and 1.4 GHz fluxes with L(IR) derived from the MIPS $24\mu\text{m}$ data only: L(IR) estimates are consistent with each other, within the uncertainties of the measured IR luminosity. We have 41 galaxies with MIPS $24\mu\text{m}$ data: 21 with detections ($S/N > 3$) and 20 with upper-limits. The redshift distribution of our final sample and subsamples are shown in Figure 1. The constraint provided by the IR luminosity allows to compute the bolometric SFR (assuming energy balance between UV and IR), and therefore the dust extinction, in an independent way. We provide more details on how we constrain galaxy physical parameters with IR data in Section 3.

To aid our analysis, we define three different subsamples: the ‘‘MIPS’’ sample (galaxies with MIPS data), the ‘‘MIPS detected’’ sample (galaxies detected at $24\mu\text{m}$ with > 3 sigma), and the ‘‘MIPS upper limit’’ sample (galaxies undetected), with 41, 21, and 20 galaxies respectively. All these galaxies have at least $H\alpha$ measurements, with 12 having $[N\ II]\ \lambda 6583$ measurements.

3. SED FITTING

Physical properties of the galaxies are inferred by fitting model SEDs to the broad-band photometry from U -band to $8\mu\text{m}$. Our SED fitting code is a modified version of the photometric redshift code *HyperZ* (Bolzonella et al. 2000). We generate a set of spectral templates with the GALAXEV code of Bruzual & Charlot (2003), for three different metallicities ($Z=0.004, 0.04, 0.02$) and three different star-formation histories (SFH=constant, exponentially rising, exponentially decreasing). The timescales used for the rising and declining SFHs are respectively $\tau_r = [10, 30, 50, 70, 100, 300, 500, 700, 1000, 3000]$ Myr and $\tau_d = [10, 30, 50, 70, 100, 300, 500, 700, 1000, 3000, \infty]$ Myr. The stellar age is defined as the age since the onset of star-formation. Unless stated otherwise, we consider a minimum age of 50 Myr corresponding to the typical dynamical timescale expected for $z \sim 2$ galaxies (e.g., Reddy et al. 2012b).

We assume that the dust attenuation is described by the Calzetti dust attenuation curve (Calzetti et al. 2000), with A_V allowed to vary from 0.0 to 6.0, in steps of 0.05. The intergalactic medium (IGM) is treated using the Madau prescription (Madau 1995). Redshifts are fixed to the spectroscopic ones. For our entire grid of models, we compute the χ^2 and

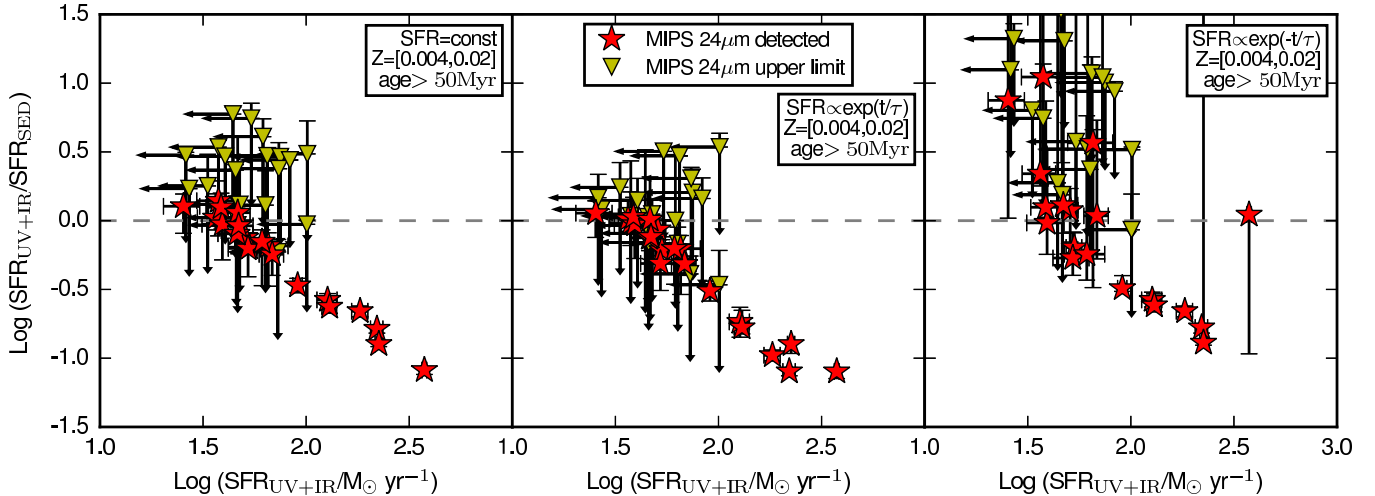


Figure 2. Comparison between $\log \text{SFR}_{\text{UV+IR}}$ and $\log(\text{SFR}_{\text{UV+IR}}/\text{SFR}_{\text{SED}})$ for three different SFHs (constant, rising, and declining, from left to right). An increasing inconsistency between $\text{SFR}_{\text{UV+IR}}$ and SFR_{SED} appears at $\text{SFR}_{\text{UV+IR}} \geq 10^{1.95} M_{\odot} \text{yr}^{-1}$ for galaxies detected in MIPS $24\mu\text{m}$. We remind that we assume energy balance in our SED fitting procedure.

the scaling factor of the template; the latter determines the SFR and M_{\star} .

We account for the effect of nebular emission (both continuum and emission lines) following Schaerer & de Barros (2009) and Schaerer & de Barros (2010). The strength of nebular emission depends mainly on the number of Lyman continuum photons, which is computed from stellar population synthesis models. Relative line intensities are taken from Anders & Fritze-v. Alvensleben (2003) and Storey & Hummer (1995), for typical ISM conditions ($n_e = 100 \text{ cm}^{-3}$, $T = 10^4 \text{ K}$). We assume that the Lyman continuum escape fraction is equal to zero, which means that our models produce the maximum theoretical strength for nebular emission for the adopted ISM physical conditions. Additionally, we assume that the same dust attenuation curve applies to the nebular and stellar emission, and that the color excess derived from the continuum applies to the line emission. If, as in the local universe, the nebular lines are subject to larger color excess than UV continuum, then our assumption would over-predict the emission line fluxes compared to the measured fluxes. Reddy et al. (2010) show that the impact of nebular emission on ages and stellar masses at $z \sim 2$ is insignificant because most of the longer wavelength bands (e.g., IRAC) used in the SED fitting are unaffected by line emission at these redshifts. Therefore our assumptions about nebular emission modeling, particularly about nebular attenuation, does not significantly affect the physical parameters derived from the SED modeling.

We also ignore the $\text{Ly}\alpha$ line contributions to the broadband fluxes because over 122 galaxies with $\text{Ly}\alpha$ flux measurements available in our sample, only one third (44) exhibits $\text{Ly}\alpha$ in emission, and more than a half of this third have $\text{EW}(\text{Ly}\alpha) < 10 \text{ \AA}$. Therefore we set the $\text{Ly}\alpha$ flux to zero in our nebular emission modeling.

We used the IR luminosity as an additional constraint to the SED fitting by assuming a balance between the energy absorbed in the UV/optical (we integrate over 912\AA to $3\mu\text{m}$), and re-radiated in the IR. *HyperZ* builds a grid of models (*Hypercube*). For each model in our grid, we compute the expected IR luminosity ($8\text{--}1000\mu\text{m}$) and then exclude from the grid all the solutions for which $L(\text{IR})_{\text{SED}}$ is inconsistent with

$L(\text{IR})_{24\mu\text{m}}$ within 68% confidence. For the non detections, we exclude solutions inconsistent with the $L(\text{IR})_{24\mu\text{m}}$ 3σ upper limits. The 41 galaxies in the MIPS sample will have the most robust determinations of SFRs and dust reddening given the independent information provided by the IR constraints. We have inspected the SED for each object to ensure that the fits are still good when assuming the energy balance: there is no significant difference between with and without energy balance (comparison based on χ^2), except for a small subsample (see Section 4.1).

Minimization of χ^2 over the entire parameter space yields the best-fit parameters. Uncertainties are determined from the χ^2 distribution, through the likelihood marginalization for each parameter of interest with $\mathcal{L} \propto \exp(-\chi^2/2)$.

4. RESULTS

In this section, we first compare the SFRs derived through SED fitting with $\text{SFR}_{\text{UV+IR}}$ (Section 4.1) and determine if the assumed Calzetti reddening curve is appropriate (Section 4.2). Because our final sample has been obtained after applying several criteria (UV-selected, optical emission line measurements), we compare the general properties of our sample with previous studies to ensure that it is representative of $z \sim 2$ star-forming galaxies (Section 4.3). We then test the ability of the SED models to reproduce observed emission line fluxes for the MIPS detected sample (Section 4.4) and explore if there is any trend among the physical parameters that could explain the discrepant results regarding the difference in color excess between nebular lines and stellar continuum found in previous studies (Section 4.5).

4.1. SFR_{SED} versus $\text{SFR}_{\text{UV+IR}}$

Figure 2 shows the comparison of the SFRs derived from SED fitting with those computed from the sum of the obscured (IR) and unobscured (UV) SFRs (the latter assume the Kennicutt 1998 relations). We find a good agreement between SFR_{SED} and $\text{SFR}_{\text{UV+IR}}$ for $\text{SFR}_{\text{UV+IR}} \lesssim 10^2 M_{\odot} \text{yr}^{-1}$ for the rising and constant SFHs: for the MIPS detected sample, the difference is $\lesssim 0.25$ dex. There is a mismatch between SFR_{SED} and $\text{SFR}_{\text{UV+IR}}$ for 7 galaxies which are the only known ultra-luminous galaxies (ULIRGs, $L(\text{IR}) > 10^{12} L_{\odot}$)

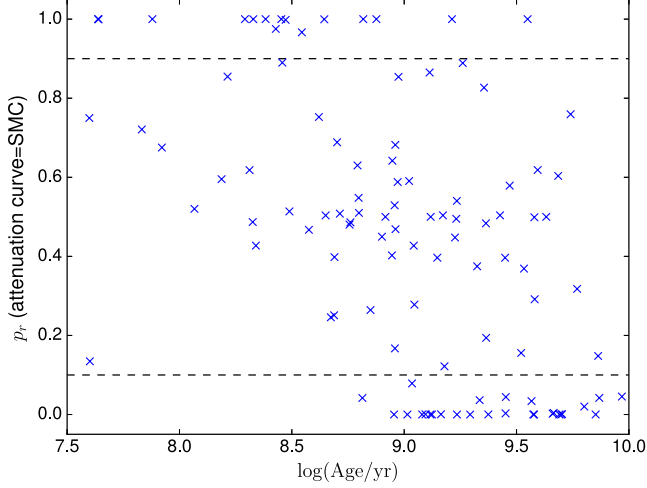


Figure 3. Relative probability for the SMC extinction curve to be the best-fit dust extinction curve versus age (also derived assuming an SMC curve). We show the result assuming a constant SFH for the entire sample. The dashed lines show the threshold we adopt when determining whether a model is the best fit one ($p_r \geq 0.9$). All galaxies above the upper line are considered best fit with the SMC curve and all galaxies below the lower line are considered best fit with the Calzetti curve. We introduce a slight offset in age to make the figure clearer.

in our sample. For these galaxies, the discrepancy between SFR_{SED} and $\text{SFR}_{\text{UV+IR}}$ is > 0.5 dex, and can be as large as ~ 1 dex. We further investigate the ULIRGs physical properties in Appendix A. The declining SFH leads to lower SFR_{SED} in comparison with $\text{SFR}_{\text{UV+IR}}$. This is consistent with the fact that declining SFHs can underpredict SFRs (e.g., Reddy et al. 2010; Wuyts et al. 2011; Reddy et al. 2012b; Price et al. 2014). In the following, we will show and discuss the results for the rising SFH mainly, since the constant and rising SFHs lead to similar results (except as indicated otherwise).

In the remainder, we present results based on SED fitting assuming energy balance, but we exclude these 7 ULIRGs from our analysis.

4.2. Attenuation curve

While we assume a Calzetti attenuation curve to perform SED fitting, Reddy et al. (2010) show that the $\text{IRX-}\beta$ relation is more consistent with an SMC-like curve (Prevot et al. 1984; Bouchet et al. 1985) than the Calzetti curve for galaxies younger than 100 Myr. To check if this is also true for our sample, we use the Akaike Information Criterion (AIC; Akaike 1974) which allows us to compare different models and derive the relative probability for one model to be the best model among a given set of models. In our case, we compare modeling assuming the Calzetti curve with those that assume the SMC curve (where all other SED parameters have been fixed in the fitting). AIC is defined as:

$$\text{AIC} = \chi^2 + 2k \quad (1)$$

where k is the number of free parameters. From the AIC, we derive the relative probability p_r for the i th model (model assuming SMC/Calzetti attenuation curve) to be the best model as:

$$\Delta_i = \text{AIC}_i - \min(\text{AIC}) \quad (2)$$

$$p_r = \frac{\exp(-1/2\Delta_i)}{\sum_i \exp(-1/2\Delta_i)} \quad (3)$$

We show the results obtained for the entire sample (Figure

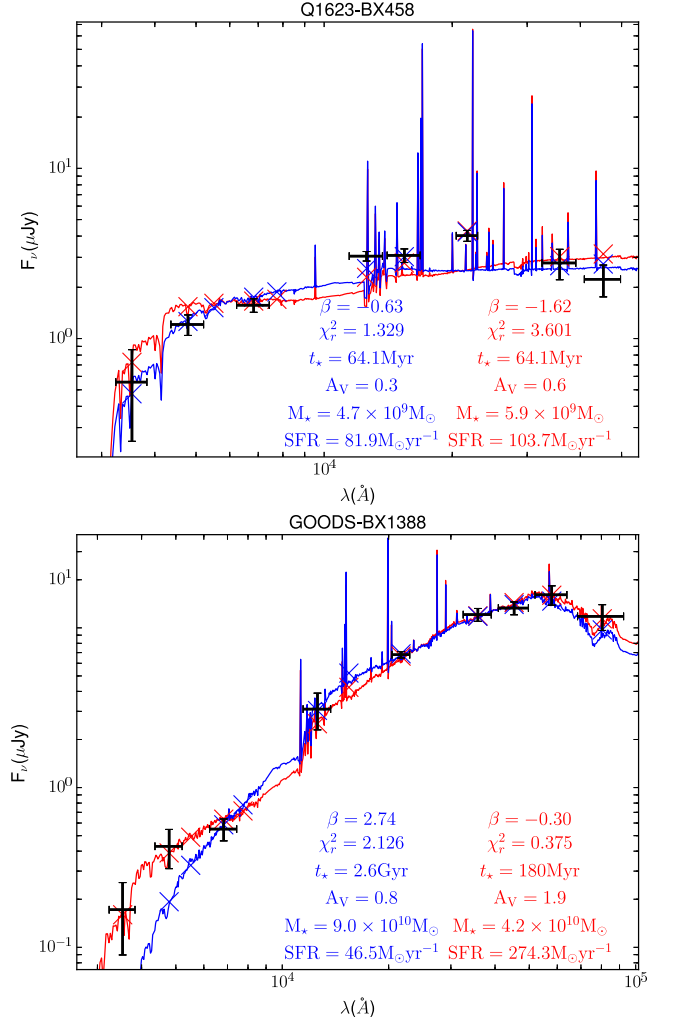


Figure 4. Observed SEDs (thick black crosses) and best-fit assuming a constant SFH with a Calzetti attenuation curve (in red) and a SMC attenuation curve (in blue) for a galaxy best fit (i.e. $p_r > 0.9$) with an SMC curve (top) and a galaxy best fit with the Calzetti curve (bottom). Thin red and blue crosses show integrated fluxes in each band. The main physical properties are shown in blue and red assuming the SMC and the Calzetti curves respectively. Apart from the use of SED fitting to discriminate among attenuation curves, it is worth noting that the K_s band excess for the galaxy Q1623-BX458 can only be explained by H α emission (Shivaei et al. 2015).

3). Since AIC is only a statistical test, we define a threshold where we consider a model as the best fit one if the relative probability is $p_r \geq 0.9$. While galaxies best fit with the SMC curve are found at any age, galaxies of a young age ($< 10^{8.5}$ years) are more likely to be fit with a SMC-like attenuation curve, while galaxies best fit with the Calzetti curve are $\gtrsim 10^9$ years. This relation between age and attenuation curve is similar to previous results in literature based on the comparison between UV to IR luminosity ratio and β slope (Reddy et al. 2006b, 2010, 2012a; Siana et al. 2008, 2009; Wuyts et al. 2012; Shivaei et al. 2015).

We show in Figure 4 two examples: one galaxy best fit with the SMC attenuation curve and one best fit with the Calzetti curve ($p_r(\text{SMC}) > 0.99$ and $p_r(\text{SMC}) < 0.01$, respectively). The main difference between the solutions obtained assuming different attenuation curves is the UV β slope ($f_\lambda \propto$

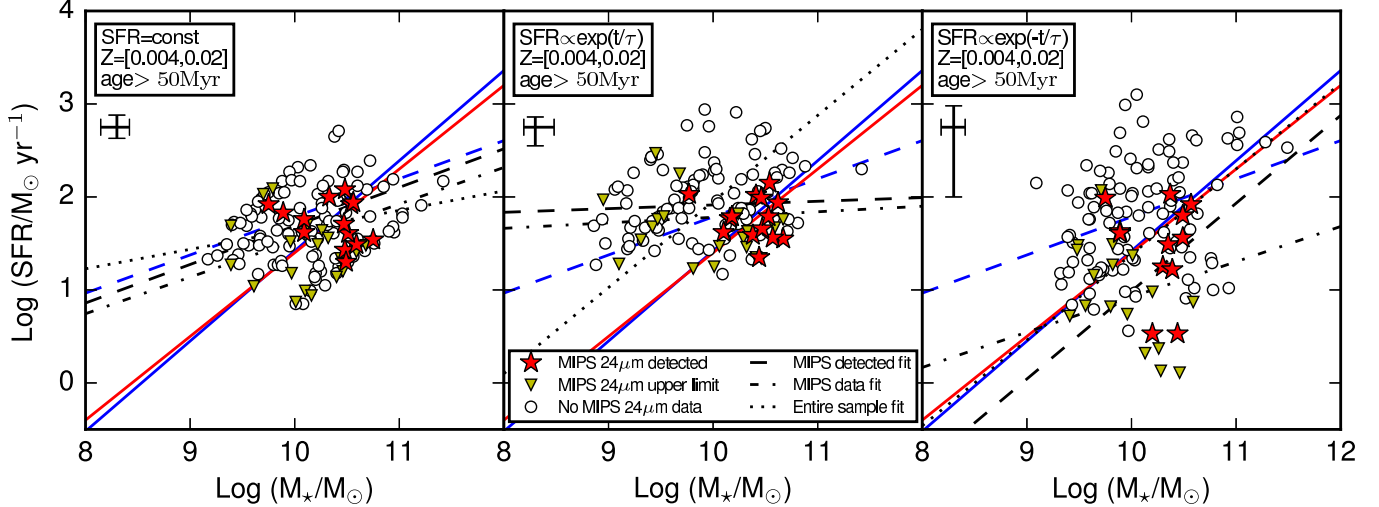


Figure 5. Star-formation rate versus stellar mass for three different star-formation histories. Star-formation rates are inferred from SED fitting assuming energy balance when MIPS $24\mu\text{m}$ data are available (see Section 3). The red and blue lines show the star formation main sequence from Daddi et al. (2007) and Reddy et al. (2012b), respectively, at $z \sim 2$. The blue dashed line shows a linear fit to the data from Reddy et al. (2012b). We show linear fits to our data for three different samples: MIPS detected (dashed lines), MIPS data (dash-dot lines) and the entire sample (dotted lines). Typical error bars are shown in the top left corner for each SFH.

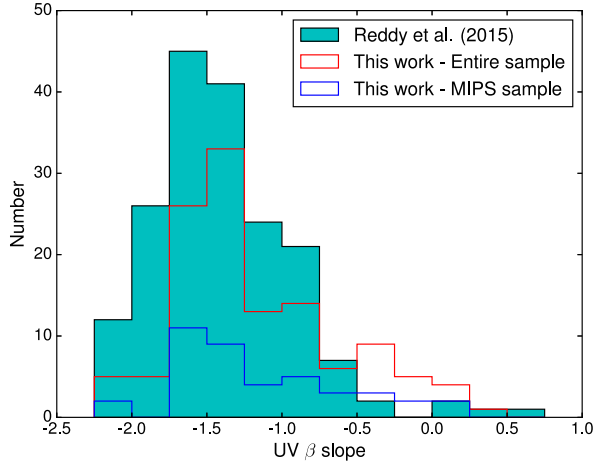


Figure 6. UV β slope distributions for the Reddy et al. (2015) sample, our entire sample, and the MIPS sample. The β slopes are derived from the observed SEDs.

λ^β). The UV β slope depends on the age and dust attenuation of the galaxy (and the SFH, Leitherer & Heckman 1995; Meurer et al. 1999). In the two examples shown, Balmer breaks are constrained by the $J-R$ color but in each case, only one attenuation curve is able to reproduce both the Balmer breaks and the UV β slopes. Best fit assuming the Calzetti curve leads to β slope bluer than the slope derived with the SMC curve. For young galaxies ($< 100\text{Myr}$), the Calzetti curve leads to β slopes too blue compared to the observed ones (Figure 4 top), while for old galaxies, the SMC curve leads to β slopes too red (Figure 4 bottom). Despite the well known degeneracy between dust attenuation and age derivation, the $J-R$ color is enough to lift the degeneracy for very young and very old galaxies, allowing to statistically discriminate between the SMC and the Calzetti curve.

According to our statistical test, the percentage of galaxies best fit with the SMC curve is $< 10\%$ of the MIPS sample (for any SFH), while galaxies best fit with the Calzetti curve represent $\sim 25\%$. The rest of the sample does not have relative probability passing our threshold, and it represents $\sim 65\%$ of

our sample. If we consider probabilities at face values, $\sim 20\%$ of the galaxies are best fit with an SMC curve and $\sim 80\%$ are best fit with a Calzetti curve. Because the majority of galaxies in our sample appears to be better described with the Calzetti curve, we assume this attenuation curve in the rest of Section 4.

4.3. General properties of the sample

In this section, we compare the properties of the MIPS sample to those of the entire sample and with the properties of $z \sim 2$ star-forming galaxies taken from the literature in order to highlight the relevance of our method and the representativeness of our sample.

The stellar masses and SFRs derived assuming a constant SFH are consistent with the relation between M_* and SFR derived in Daddi et al. (2007) and Reddy et al. (2012b), with a rms scatter of 0.37 dex as in Reddy et al. (2012b) (Figure 5). The rms scatter for the rising and the declining SFHs are 0.56 and 0.75 dex, respectively. Using a Spearman correlation test, we find that SFR and M_* are weakly correlated (the strongest correlation is found for the declining SFH, with $\rho = 0.22$ and $\sigma = 2.56$). We perform linear fits to our sample and subsamples (total MIPS sample and the MIPS-detected sample). While the stellar masses and SFRs for the MIPS detected sample do not depend strongly on the assumed star formation history, for galaxies without MIPS data the effect of star-formation history is more important. While ages derived with the rising star formation histories are similar to those derived assuming a constant SFH ($\overline{\Delta(\log \text{Age})} = 0.0$, $\sigma = 0.2$), dust extinctions are higher relative to the ones derived with the constant SFH ($\overline{\Delta(\log A_V)} = 0.2$, $\sigma = 0.2$). Accordingly the SFRs are also higher ($\overline{\Delta(\log \text{SFR})} = 0.3$, $\sigma = 0.3$, see also Schaefer & Pelló 2005; de Barros et al. 2014). For objects in the MIPS sample, the differences in SED parameters obtained with different SFHs are reduced relative to those derived when no IR constraints are available.

While deriving the relation between SFR and M_* at $z \sim 2$ is not the main focus of this paper, our method used to derive physical properties of galaxies leads to results consistent

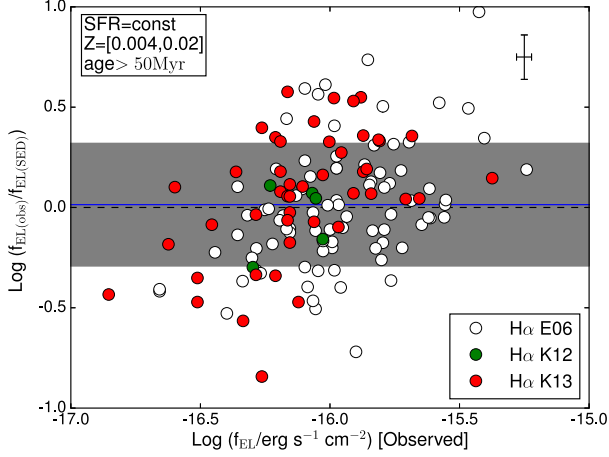


Figure 7. Comparison between $\log f_{\text{EL}(\text{obs})}$ and $\log(f_{\text{EL}(\text{obs})}/f_{\text{EL}(\text{SED})})$ for the entire sample. Emission line fluxes are taken from Erb et al. (2006b), Kulas et al. (2012), and Kulas et al. (2013), hereafter E06, K12, and K13 respectively. The blue line shows the median $\log(f_{\text{EL}(\text{obs})}/f_{\text{EL}(\text{SED})})$ value and the grey area the 1σ dispersion.

Errors are determined by combining measurement error of the observed fluxes with the errors derived from parameter degeneracy (black cross in the right top corner).

with what we expect for typical $z \sim 2$ star-forming galaxies in terms of their SFRs and stellar masses, if we assume a constant SFH.

To assess if our sample is biased in terms of dust properties, we compare observed UV β slopes from the sample from Reddy et al. (2015) with the slopes of our sample in Figure 6. We derive the slopes using the filters probing the rest-frame range $\lambda = 1500 - 2500\text{\AA}$ (e.g., Castellano et al. 2012). Both our entire and MIPS samples exhibit distributions similar to the Reddy et al. (2015) sample, with a small galaxy fraction probing redder β slopes ($\beta > -0.5$).

Thus, our sample is likely representative of $> 10^9 M_{\odot}$ $z \sim 2$ galaxies in general.

4.4. Reproducing emission line fluxes

We now compare the emission line fluxes predicted by our SED fitting code (see Section 3) with the observed emission line fluxes. We mainly study the results for the $\text{H}\alpha$ line because we have $\text{H}\alpha$ measurements for 137 galaxies allowing for significant statistics. Furthermore, the $[\text{N II}] \lambda 6583$ to $\text{H}\beta$ flux ratio depends strongly on metallicity with $F_{[\text{N II}] \lambda 6583}/F_{\text{H}\beta} = 0.175$ for $Z = 0.004$ and $F_{[\text{N II}] \lambda 6583}/F_{\text{H}\beta} = 0.404$ for $Z = 0.02$, while the $[\text{O III}] \lambda 5007$ to $\text{H}\beta$ flux ratio is less metallicity dependent ($F_{[\text{O III}] \lambda 5007}/F_{\text{H}\beta} = 4.752$ and $F_{[\text{O III}] \lambda 5007}/F_{\text{H}\beta} = 4.081$ for $Z = 0.004$ and $Z = 0.02$, respectively, Anders & Fritze-v. Alvensleben 2003), but more sensitive to the H II physical conditions like ionization parameter or leakage of ionizing photons (e.g., Kewley et al. 2013a; Nakajima & Ouchi 2014).

To quantify this comparison, we computed $\Delta f_{\text{EL}} = \log(f_{\text{EL}(\text{obs})}/f_{\text{EL}(\text{SED})})$, where $f_{\text{EL}(\text{obs})}$ is the observed emission line flux and $f_{\text{EL}(\text{SED})}$ is the SED predicted emission line flux. We remind the reader that the SED fitting assumes that the color excesses of the nebular regions and the stellar continuum are equal, i.e., $E(\text{B}-\text{V})_{\text{stellar}} = E(\text{B}-\text{V})_{\text{nebular}}$ (derived assuming the Calzetti extinction curve). Under this assumption, the $\text{H}\alpha$ extinction is $A_{\text{H}\alpha} = 3.33 \times E(\text{B}-\text{V})_{\text{stellar}}$. The comparison between our predicted and observed fluxes for the entire

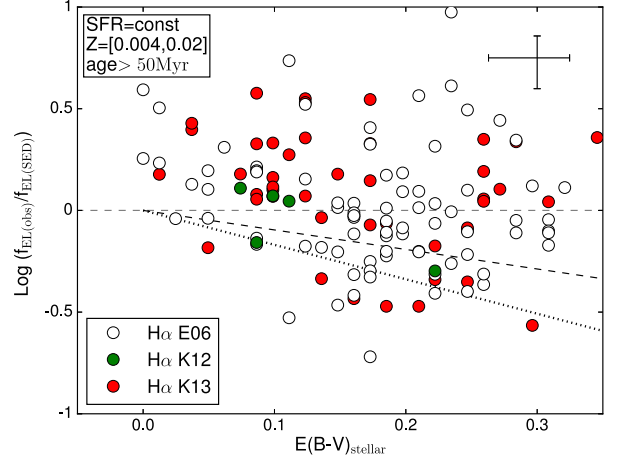


Figure 8. $\Delta \log f_{\text{EL}}$ vs. $E(\text{B}-\text{V})_{\text{stellar}}$ for the entire sample. The dashed line and the dotted line show the expected relation from equation 5 and equation 6, respectively.

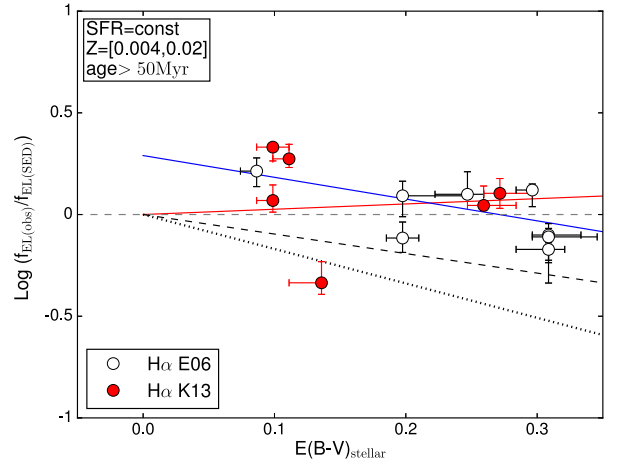


Figure 9. Same as Fig. 8 for the MIPS detected sample. We show 2 different fits to the $\text{H}\alpha$ data: in blue, we show a linear fit to the data, with the slope and intercept as free parameters. Additionally, in red, we show the linear fit where we fix the intercept to be zero.

sample is shown in Figure 7. We assume a constant SFH because this SFH provides the best match to the $z \sim 2$ galaxy physical properties (Sect. 4.3). On average, our method used to model nebular emission from the photometry provides $\text{H}\alpha$ fluxes consistent with observations: the median shows a slight underprediction of the flux by $\sim 3\%$ with $\sigma = 0.31$ dex.

We first study how $\Delta \log f_{\text{EL}}$ correlates with the stellar color excess (Figure 8). We compare our results with the relationship between nebular and color excess for local galaxies⁶ from Calzetti et al. (2000):

$$E(\text{B}-\text{V})_{\text{stellar}} = (0.44 \pm 0.03) \times E(\text{B}-\text{V})_{\text{nebular}} \quad (4)$$

The extinction at a wavelength λ is related to the color excess $E(\text{B}-\text{V})$ and to reddening curve $k(\lambda)$ by $A_{\lambda} = k(\lambda) \times E(\text{B}-\text{V})$. At the $\text{H}\alpha$ wavelength (6562.8\AA), we have $k_{\text{Calzetti}}(\text{H}\alpha) = 3.33$ and $k_{\text{Cardelli}}(\text{H}\alpha) = 2.52$, which leads re-

⁶ Equation 4 is often misinterpreted as both color excesses being derived with the same attenuation curve, but the intent was that the nebular regions are described by a line-of-sight (e.g., Milky Way) extinction curve (e.g., Steidel et al. 2014; Reddy et al. 2015).

spectively in terms of $H\alpha$ extinction (assuming Equation 4):

$$A_{H\alpha, \text{Cardelli}} = 5.72 \times E(B-V)_{\text{stellar}} \quad (5)$$

$$A_{H\alpha, \text{Calzetti}} = 7.55 \times E(B-V)_{\text{stellar}} \quad (6)$$

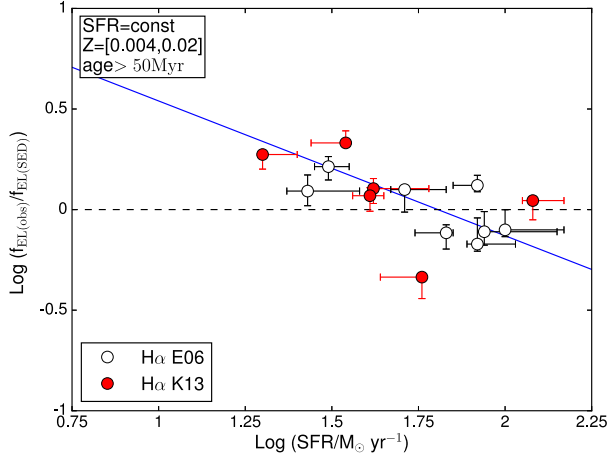


Figure 10. $\Delta \log f_{\text{EL}}$ vs. SFR for the MIPS detected sample. Linear fit to the data is shown with the blue line.

Our comparison between predicted fluxes (based on SFR_{SED} derived assuming energy balance) and observed fluxes should allow us to discriminate between equations 5 and 6. If the relative color excess of the UV continuum and the nebular emission lines at $z \sim 2$ is similar to the one derived in local starburst galaxies, we expect to overpredict emission line fluxes because we assume $A_{V, \text{nebular}} = A_{V, \text{stellar}}$. Furthermore, if the nebular color excess is related to UV color excess as in local starburst galaxies (i.e., $E(B-V)_{\text{nebular}} = \text{constant} \times E(B-V)_{\text{stellar}}$), we should find an anticorrelation between $\Delta \log f_{\text{EL}}$ and $E(B-V)_{\text{stellar}}$. If we assume, as we do in our SED fitting procedure, that the same attenuation curve applies to both nebular and stellar emission, we get:

$$\frac{f_{\text{EL}(\text{obs})}}{f_{\text{EL}(\text{SED})}} = \frac{f_{\text{intrinsic}} \times 10^{-0.4 \times A_{\lambda(\text{obs})}}}{f_{\text{intrinsic}} \times 10^{-0.4 \times A_{\lambda(\text{SED})}}} \quad (7)$$

$$\log \left(\frac{f_{\text{EL}(\text{obs})}}{f_{\text{EL}(\text{SED})}} \right) = -0.4 \times (A_{\lambda(\text{obs})} - A_{\lambda(\text{SED})}) \quad (8)$$

$$\Delta \log f_{\text{EL}} = -0.4 \times k(\lambda) \times (E(B-V)_{\text{neb}} - E(B-V)_{\text{stel}}) \quad (9)$$

A Spearman correlation test performed on data from Figure 8 leads to $\rho = -0.31$ with standard deviation from null hypothesis $\sigma = 3.63$ (Table 1), which indicates that $\Delta \log f_{\text{EL}}$ and $E(B-V)_{\text{stellar}}$ are possibly anticorrelated. We also compare the results expected from equation 5 and equation 6 with our data. While our method is able to reproduce observed emission lines within a factor $\lesssim 2$, uncertainties remain too large to derive a possible relation between $E(B-V)_{\text{stellar}}$ and $\Delta \log f_{\text{EL}}$. To decrease the uncertainties, we focus on the MIPS detected sample (Fig. 9). We compare the results expected from equation 5 and equation 6 with linear fits to our data:

$$\Delta \log f_{\text{EL}} = a \times E(B-V)_{\text{stellar}} + b \quad (10)$$

and we perform two linear fits:

- (1) We fit the MIPS detected sample (blue in Figure 8).

- (2) We fit the MIPS detected sample assuming $b = 0$ in equation 10 (red).

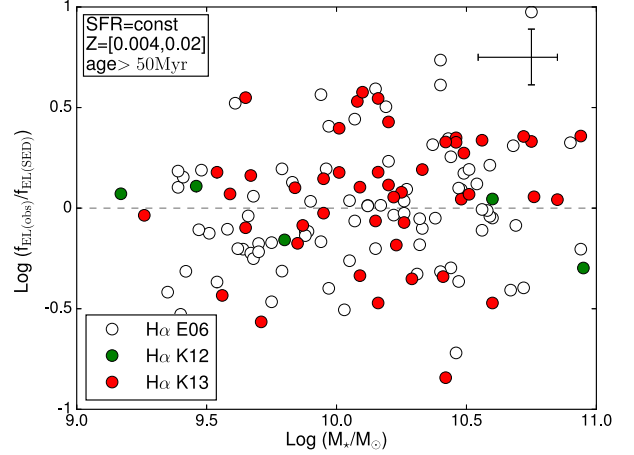


Figure 11. $\Delta \log f_{\text{EL}}$ vs. M_* for the entire sample. Typical error bar is shown in the top right corner.

Assuming $b = 0$ means that we consider that our SED fitting code is able to reproduce the emission line fluxes for dust free galaxies. The intercept of fit (1) means that we underestimate observed emission line fluxes for dust free galaxies by a factor ~ 2 . When assuming $b = 0, E(B-V)_{\text{stellar}}$ and $E(B-V)_{\text{nebular}}$ are similar (assuming a Calzetti extinction curve for both emission). This result is consistent with the conclusion from Shivaei et al. (2015). However, fit (1) shows that we are not predicting exactly emission fluxes for galaxies with no extinction. If we assume that there is a systematic offset between predicted and observed fluxes, not dependent on $E(B-V)_{\text{stellar}}$, we can compare the slope of our relation with expectation from equation 5 and 6. Then, our slope is consistent with equation 5.

4.5. Relation between nebular color excess and other physical properties

In this section we determine whether $\Delta \log f_{\text{EL}}$ possibly correlates with other physical properties such as SFR, M_* , and sSFR. We summarize the correlation test and their associated significances for the different samples in Table 1.

We find an anticorrelation between $\log \text{SFR}$ and $\Delta \log f_{\text{EL}}$ with a level of confidence $> 6\sigma$ ($\rho = -0.53$, $\sigma = 6.67$). This relation could explain the discrepancies among different previous studies. We derive the relation between $\Delta \log f_{\text{EL}}$ and $\log \text{SFR}$ using the MIPS detected sample because uncertainties are too large when IR information is missing. Assuming a constant SFH, the relation from Figure 10 implies:

$$E(B-V)_{\text{stellar}} - E(B-V)_{\text{nebular}} = (-0.50 \pm 0.10) \times \log \text{SFR} + (0.91 \pm 0.18) \quad (11)$$

This anticorrelation between $\Delta \log f_{\text{EL}}$ and $\log \text{SFR}$ implies that for $z \sim 2$ star-forming galaxies with $\log \text{SFR} \leq 1.82_{-0.60}^{+0.90}$, we have $E(B-V)_{\text{stellar}} \sim E(B-V)_{\text{nebular}}$. While uncertainty is large, this result is consistent with the SFR value derived in Reddy et al. (2015). We discuss this point further in Section 5.3.

We find no correlation between M_* and $\Delta \log f_{\text{EL}}$ (Fig. 11), with $\rho = 0.16$ and $\sigma = 1.86$. On the contrary, we find an anticorrelation between sSFR and $\Delta \log f_{\text{EL}}$ with $\rho = -0.52$ and

$\sigma = 6.48$ (Fig. 12). Again, the uncertainties are too large to derive a relation between $\Delta \log f_{\text{EL}}$ and $\log \text{sSFR}$ for the entire sample, and we use the MIPS detected sample to derive a relation. From Figure 12, we get:

$$E(B-V)_{\text{stellar}} - E(B-V)_{\text{nebular}} = (-0.31 \pm 0.07) \times \log(\text{sSFR}) + (0.16 \pm 0.03) \quad (12)$$

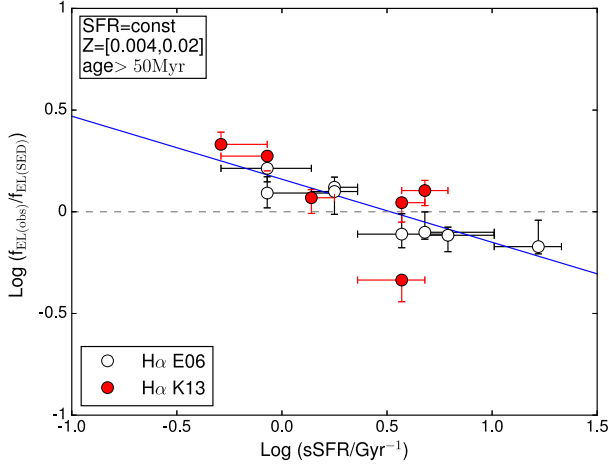


Figure 12. $\Delta \log f_{\text{EL}}$ vs. sSFR for the MIPS detected sample. Linear fit to the data is shown with the blue line.

We conclude that the analysis of our sample supports marginally the relation derived between $E(B-V)_{\text{stellar}}$ and $E(B-V)_{\text{nebular}}$ in local star-forming galaxies (Eq. 5, Calzetti et al. 2000). While we do not find a correlation between the stellar mass and $E(B-V)_{\text{stellar}} - E(B-V)_{\text{nebular}}$, we find anticorrelations between SFR/sSFR and $E(B-V)_{\text{stellar}} - E(B-V)_{\text{nebular}}$ (Reddy et al. 2015).

5. DISCUSSION

5.1. Modeling of nebular emission

One result of our study is that our SED fitting code is able to reproduce consistently the broad-band photometry and emission line fluxes, within their respective uncertainties, if we assume energy balance. This result is not a trivial finding as our modeling of the nebular emission relies on several assumptions regarding the Lyman continuum escape fraction, ISM physical conditions, empirical ratios between emission lines, and the IMF.

However, we can not rule out that a different set of physical properties could produce similar emission line fluxes. For example, the $\text{H}\alpha$ flux would decrease by a factor 1.8 if we consider a Chabrier IMF (Chabrier 2003) instead of a Salpeter IMF. Furthermore, the absolute flux of hydrogen emission lines are directly proportional to the number of ionizing photons per second, and so to the Lyman continuum escape fraction (e.g., Krueger et al. 1995). Nevertheless, we show in Figure 13 the comparison between predicted and observed $[\text{O III}] \lambda 5007$ and $[\text{N II}] \lambda 6583$ fluxes. We have shown in the previous sections that the effect of difference between nebular and stellar color excesses is negligible in the range of SFR (and sSFR) probed with our sample. Therefore, $\Delta \log f_{\text{EL}}$ for these two lines is mostly sensitive to the metallicity for $[\text{N II}] \lambda 6583$ (from Z_{\odot} to $0.2Z_{\odot}$ the $[\text{N II}] \lambda 6583/\text{H}\alpha$ ratio decreases by a factor 2.34,

Anders & Fritze-v. Alvensleben 2003), and to the ISM physical conditions for $[\text{O III}] \lambda 5007$ (e.g., Kewley et al. 2013a). Our method is able to reproduce these lines with a similar accuracy as it reproduces $\text{H}\alpha$, with a median $\Delta \log f_{\text{EL}} \sim 0$ and $\sigma = 0.34$ dex.

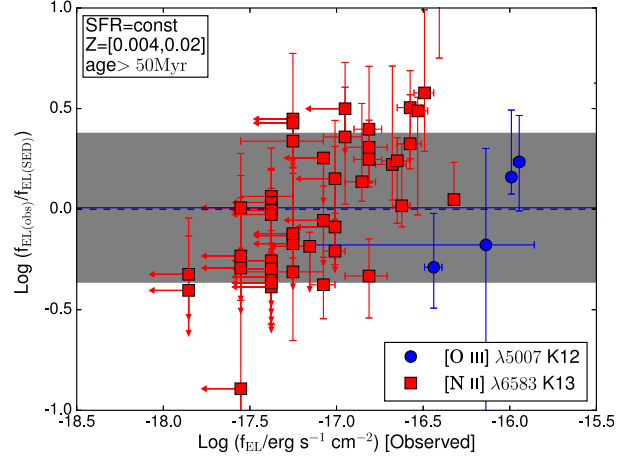


Figure 13. Same as Figure 7 for the $[\text{N II}] \lambda 6583$ and $[\text{O III}] \lambda 5007$ measurements. The blue line shows the median $\Delta \log f_{\text{EL}}$ value and the grey area the 1σ dispersion.

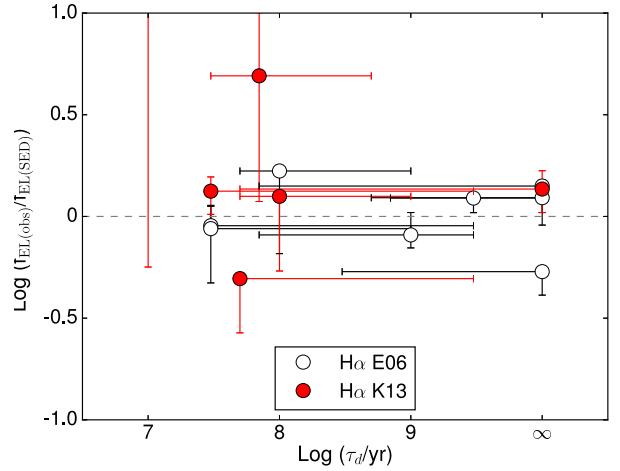


Figure 14. $\Delta \log f_{\text{EL}}$ vs. timescale τ_d for the MIPS detected sample assuming a declining star-formation history. We show the result only for the $\text{H}\alpha$ data for more clarity.

We show that the method used in this work to model nebular emission (Schaerer & de Barros 2009, 2010) is able to reproduce $\text{H}\alpha$, $[\text{N II}] \lambda 6583$, and $[\text{O III}] \lambda 5007$. This is an important result because of the implications for higher redshift studies ($z > 3$), where emission lines can not be measured with current instruments while observed SEDs exhibit evidences of impact of nebular emission (e.g., Stark et al. 2013; de Barros et al. 2014; Nayyeri et al. 2014; Marmol-Queralto et al. 2015; Smit et al. 2015).

5.2. Star-formation history

Several studies have used the comparison between direct star-formation tracers and $\text{SFR}(\text{SED})$ to put constraints on star-formation timescales. Their main conclusion is that declining SFHs result in $\text{SFR}(\text{SED})$ that are inconsistent with

Table 1
Spearman correlation test between $\Delta \log f_{\text{EL}}$ and physical parameters

| Physical parameters | MIPS detected ($N = 14$) | | MIPS sample ($N = 34$) | | Entire sample ($N = 137$) | |
|---------------------------|----------------------------|------------|--------------------------|----------|-----------------------------|----------|
| | ρ^a | σ^b | ρ | σ | ρ | σ |
| $E(B-V)_{\text{stellar}}$ | -0.46 | 1.61 | -0.35 | 1.96 | -0.31 | 3.63 |
| SFR | -0.62 | 2.31 | -0.78 | 5.68 | -0.53 | 6.67 |
| M_* | 0.66 | 2.58 | 0.13 | 0.73 | 0.16 | 1.86 |
| sSFR | -0.76 | 3.21 | -0.57 | 3.49 | -0.52 | 6.48 |

^a Spearman rank correlation coefficient.

^b Standard deviations from null hypothesis.

those inferred from multi-wavelength tracers of star formation (e.g., the sum of the IR and UV), or that it is necessary to assume a lower limit on the decay timescale ($\tau_d \gtrsim 300\text{Myr}$; Wuyts et al. 2011; Reddy et al. 2012b; Price et al. 2014). To gain insight on the star-formation timescales for both rising and declining SFHs, we rely on the MIPS detected sample since the SFR uncertainties are much lower when L(IR) is used to perform SED fitting assuming energy balance (the uncertainties derived from SED fitting are 0.1 dex versus 0.35 dex without assuming energy balance). Therefore, we use both IR and emission lines to place constraints on the SFH timescale (Schaerer et al. 2013).

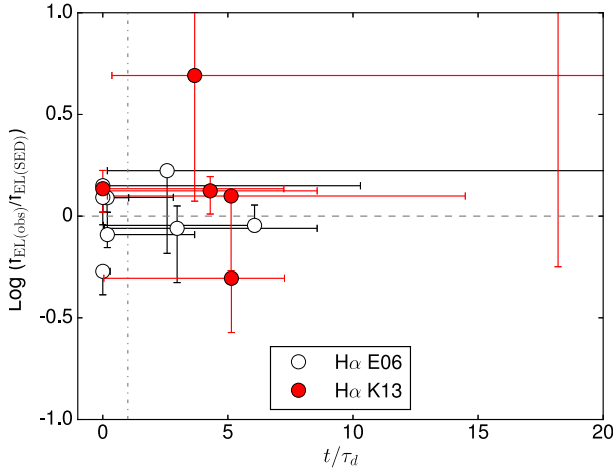


Figure 15. $\Delta \log f_{\text{EL}}$ vs. the ratio between age and timescale t/τ_d for the MIPS detected sample assuming a declining star-formation history and a relation between $E(B-V)_{\text{nebulular}}$ and $E(B-V)_{\text{stellar}}$ described by Equation 11. The dash-dotted line shows $t/\tau_d = 1$. We show the result only for the $H\alpha$ data for more clarity

Since we assume energy balance, the IR luminosity predicted from SED fitting are consistent with $L(\text{IR})_{24\mu\text{m}}$ by construction. The difference between predicted and observed emission lines fluxes assuming a declining SFH do not differ significantly from other SFHs, except for galaxies with blue stellar color excess. In Figure 14, we show the relation between $\Delta \log f_{\text{EL}}$ and the timescale τ_d and in Figure 15, the relation between $\Delta \log f_{\text{EL}}$ and the ratio between age and timescale t/τ_d . Overall, the SED fitting reproduces the observed $H\alpha$ fluxes with the same accuracy as for the entire sample (i.e., the fluxes are reproduced within a factor 2). There are two galaxies for which the fluxes are significantly underpredicted ($\Delta \log f_{\text{EL}} > 0.5$) and they are fit with short timescales ($\leq 100\text{Myr}$). In Figure 15, we see that the age to timescale ratio can be as high as ~ 5 with the predicted emission line fluxes still consistent with the observed values. The two galaxies for which we significantly underpre-

dict the emission line fluxes have the lowest IR luminosities of the sample ($\leq 10^{11}L_{\odot}$). If we add the $H\alpha$ flux measurement constraints to the SED fit for these two galaxies (excluding solutions providing $H\alpha$ fluxes inconsistent with the observed ones within 1σ), timescales are $\tau_d \geq 500\text{Myr}$ and the age to timescale ratios are $t/\tau_d < 1$. Our conclusions regarding declining SFHs are consistent with the literature (e.g., Wuyts et al. 2011; Price et al. 2014) but for a fraction of our MIPS detected sample ($\sim 1/3$), we find that galaxy SEDs are fit with short timescales ($30\text{Myr} \leq \tau_d \leq 1\text{Gyr}$) and relatively large t/τ_d ratios ($0 \leq t/\tau_d \leq 5$), and have predicted physical quantities (L(IR) and $H\alpha$ flux) consistent with observations.

We overpredict the emission line fluxes for objects fit with a short exponential timescale ($\tau_r < 10^8\text{yr}$) for the rising SFH (data not shown), while we underpredict fluxes for fit with a large timescale ($> 10^9\text{yr}$).

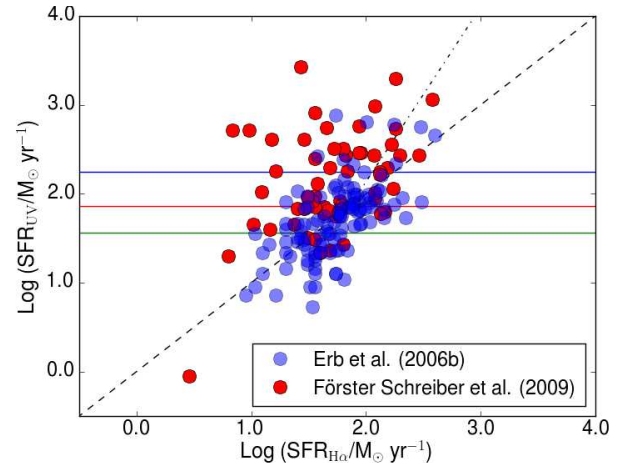


Figure 16. $\text{SFR}_{H\alpha}$ vs. SFR_{UV} assuming $E(B-V)_{\text{stellar}} = E(B-V)_{\text{nebulular}}$ for the Erb et al. (2006a) and Förster Schreiber et al. (2009) samples. The horizontal red line shows $\log \text{SFR} = 1.82$ (Section 4.5, Equation 11), the blue line $\log \text{SFR} = 2.25$ (Yoshikawa et al. 2010), and the green line $\log \text{SFR} = 1.56$ (Reddy et al. 2015, converting the value from a Chabrier to a Salpeter IMF). The dash-dotted line is the expected $\log \text{SFR}(H\alpha) - \log \text{SFR}(UV)$ relation assuming that $E(B-V)_{\text{nebulular}} - E(B-V)_{\text{stellar}}$ is related to $\log \text{SFR}$ as described in Equation 11. The dashed line is the one to one relation.

To perform SED fitting and get results consistent with observed emission line fluxes, assuming energy balance (and so having IR information), we show that the timescale used with a declining SFH is $\tau_d \geq 30\text{Myr}$ and that the age to timescale ratio is ≤ 5 . For a rising SFH, the timescale is in the range $300\text{Myr} \leq \tau_r \leq 1\text{Gyr}$.

5.3. Comparison with other studies

We find an anticorrelation between SFR and $\Delta \log f_{\text{EL}}$ which we interpret as a correlation between SFR and

$E(B-V)_{\text{stellar}} - E(B-V)_{\text{nebular}}$ (Equation 11): the nebular color excess becomes larger than the stellar color excess with increasing SFR. As pointed out by Reddy et al. (2010), previous studies included galaxies with different ranges in SFR and M_* . Therefore we check now if our relation found between SFR and $\Delta \log f_{\text{EL}}$ could explain the discrepant results on this matter.

We compare the Erb et al. (2006a) sample, for which the nebular and stellar color excesses are similar, and the Förster Schreiber et al. (2009) sample, for which the nebular color excess is higher than the stellar color excess (Equation 4). It is worth noting that a fraction of our sample is drawn from the Erb et al. (2006a) sample.

We show in Figure 16 the comparison between SFR_{UV} and $\text{SFR}_{\text{H}\alpha}$ for these two studies assuming $E(B-V)_{\text{stellar}} = E(B-V)_{\text{nebular}}$, a Calzetti attenuation curve, and after converting the SFRs from a Chabrier IMF to a Salpeter IMF. We expect to see an increasing discrepancy between $\text{SFR}_{\text{H}\alpha}$ and SFR_{UV} above the value derived from Equation 11 with $\log \text{SFR} = 1.82$. We also show similar SFR thresholds found in Yoshikawa et al. (2010) and (Reddy et al. 2015).

Because we do not have Balmer decrement measurements in order to correct $\text{H}\alpha$, we consider the dust-corrected SFR_{UV} as the one with which we compare $\text{SFR}_{\text{H}\alpha}$. We can predict the difference between $\text{SFR}(\text{H}\alpha)$ derived assuming $E(B-V)_{\text{stellar}} = E(B-V)_{\text{nebular}}$ and $\text{SFR}(\text{H}\alpha)$ derived assuming the relation between SFR and the difference in the color excesses as in Equation 11 (dash-dotted line in Figure 16). At $\log \text{SFR} = 1.82$, this difference is zero and reach 0.56 dex at $\text{SFR}(\text{UV})_{\text{corrected}} = 10^3 M_{\odot} \text{yr}^{-1}$. This explains why we do not see any significant discrepancy between $\text{SFR}(\text{UV})$ and $\text{SFR}(\text{H}\alpha)$ in Figure 16 below the SFR limit derived in Yoshikawa et al. (2010). Assuming $E(B-V)_{\text{stellar}} = E(B-V)_{\text{nebular}}$ leads to underpredict $\text{SFR}_{\text{H}\alpha}$ in comparison with SFR_{UV} above the threshold found in Yoshikawa et al. (2010). Therefore we conclude that the discrepant result about the difference between nebular and stellar color excesses is likely a selection effect, the Förster Schreiber et al. (2009) sample probing higher SFRs. The apparent discrepancy between Equation 11 and the Förster Schreiber et al. (2009) sample can be explained by the large dispersion in color excess for individual galaxies (Reddy et al. 2015).

6. CONCLUSIONS

We use a sample of 149 star-forming galaxies spectroscopically confirmed at $z \sim 2$ with optical emission line measurements to investigate the relative dust attenuation of the UV continua and the nebular emission in these galaxies. For a subsample of 41 galaxies, MIPS $24\mu\text{m}$ data are available and we use them to derive the infrared luminosity of these galaxies. We compare all the available observed/derived properties of our sample (emission line flux, IR luminosity) with predictions from stellar population synthesis models, taking into account nebular emission, and assuming energy balance between UV and IR emission. We explore a large parameter space, exploring different star-formation histories (constant, declining, rising) and the impact of different attenuation curves (Calzetti and SMC curves) on our results.

We compare the properties (stellar masses, SFRs) of our sample with properties found in literature (Daddi et al. 2007; Reddy et al. 2012a) to ensure the representativeness of our sample. It appears that we are not able to reproduce the observed UV β slope for the ULIRGs in our sample when we assume energy balance and we exclude these 7 galaxies from

our analysis. Our results confirm that the Calzetti curve is not appropriate for ULIRGs (Appendix A) and an appropriate attenuation curve should be define to derive properly their physical properties (Reddy et al. 2010; Casey et al. 2014).

Our conclusions are as follow:

- Assuming energy balance, our SED fitting code is able to reproduce the observed emission line fluxes for galaxies in our sample (within a factor < 2).
- Young galaxies (≤ 100 Myr) are statistically better fit with an SMC curve rather than a Calzetti curve (Reddy et al. 2010).
- We find a correlation between SFR and $E(B-V)_{\text{stellar}} - E(B-V)_{\text{nebular}}$, and also between sSFR and $E(B-V)_{\text{stellar}} - E(B-V)_{\text{nebular}}$. The color excess difference increases with increasing SFR and sSFR. The correlation between the amount of extra attenuation toward nebular emission and the SFR could explain discrepancies among previous studies about the nebular attenuation relative to stellar attenuation (e.g., Erb et al. 2006a; Förster Schreiber et al. 2009; Reddy et al. 2010).
- We use SED, IR and emission line flux measurements to constrain the star formation history. Overall, a large range of SFHs can reproduce the observables. We find that assuming a declining SFH, the timescale is $\tau_d > 30\text{Myr}$ and the age to timescale ratio is $t/\tau_d \leq 5$. For a rising SFH, the timescale is $300\text{Myr} \leq \tau_r \leq 1\text{Gyr}$.

We look forward to comparing our results with current ongoing survey (Reddy et al. 2015). This will also allow to determine much more precisely the ratio $E(B-V)_{\text{stellar}}/E(B-V)_{\text{nebular}}$, and determine if there is an evolution of this ratio from low to high redshift. However, our results suggest that this kind of observations must aim a large range of SFRs and stellar masses to avoid any bias. It would also be interesting to measure Balmer decrement of ULIRGs to derive the best method to infer their physical properties such as stellar mass, SFR, and dust attenuation.

We thank the referee for suggestions that clarify the text and the analysis. S. D. B. was supported by a fellowship from the Swiss National Science Foundation. We thank the referee for suggestions that clarify the text and the analysis. We acknowledge Chuck Steidel and his group for help in obtaining the data presented here. We thank Alice Shapley, Valentino González, Pascal Oesch, Bahram Mobasher, Daniel Schaerer, Panos Sklias, Alberto Domínguez, and Matthew Hayes for useful discussions about this work. We also thank Roser Pelló, Daniel Schaerer, and Panos Sklias for their support with *HyperZ*.

A. ULIRG PHYSICAL PROPERTIES

As shown in Figure 2, for the ULIRGs, the SFRs derived from SED fitting are inconsistent with those derived from UV and IR luminosity. The mismatch between $\text{SFR}_{\text{UV+IR}}$ and SFR_{SED} arises from the inability of our SED fitting code to reproduce both the derived IR luminosity and the observed UV β slope. UV β slope can be used to derive the dust attenuation assuming an attenuation curve for typical (i.e., L^*) galaxies at high-redshift (e.g., Reddy et al. 2010). We show

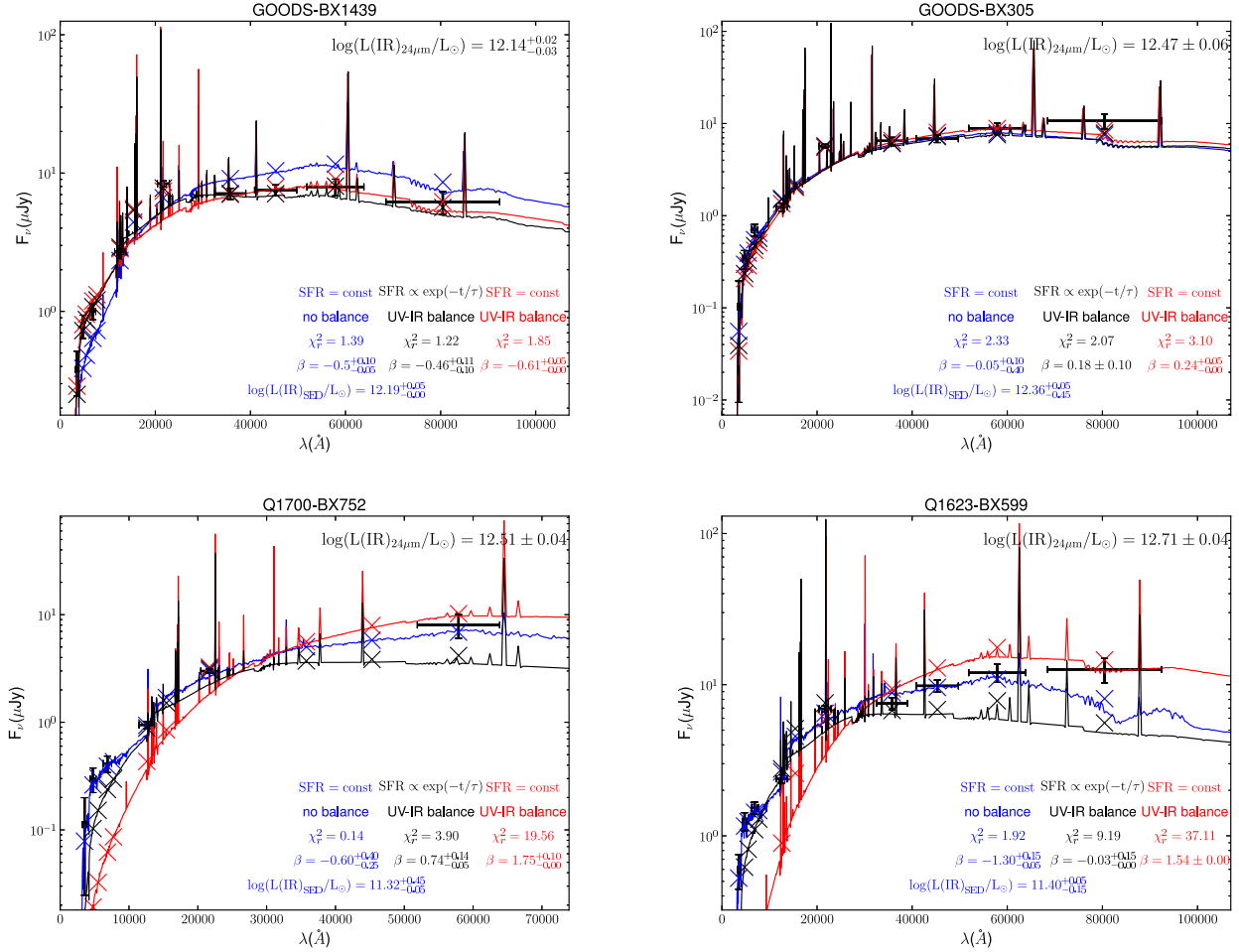


Figure 17. Observed SEDs (black thick points) of the seven ULIRGs in our sample with the best-fits for three models: constant SFH, age > 50 Myr, and $Z = [0.004, 0.02]$ (blue); constant SFH, age > 50 Myr, $Z = [0.004, 0.02]$, and assuming energy balance between UV and IR (red); and declining SFH, age free, $Z = [0.0004, 0.004, 0.02]$, and assuming energy balance (black). Crosses show the synthesised flux in the filters. For each model and galaxy, we show the χ^2_r , the UV β slope associated with the best-fit solution, and the predicted infrared luminosity when relevant.

in Figure 17 the SED fits of the seven ULIRGs in our sample for three different models: two assuming a constant SFH, with and without assuming energy balance, and one assuming a declining SFH with relaxed assumptions on age and metallicity, and assuming energy balance. This latter model is used because it is the model with the maximum number of degrees of freedom and should be more able to reproduce the SED.

The observed β slopes are bluer than what we would expect given the high IR luminosities, assuming a Calzetti curve (Meurer et al. 1999; Calzetti et al. 2000). This is also consistent with the better agreement between SFR_{SED} and $\text{SFR}_{\text{UV+IR}}$ for the ULIRGs assuming a declining SFH and a large range of ages and metallicities: the β slope is more sensitive to change in age and metallicity for a declining SFH than for a constant SFH (Leitherer & Heckman 1995). Indeed, relaxing assumptions on age and metallicity for the declining SFH leads to slightly younger ages (age > 30 Myr) and SED fits with the minimum allowed metallicity ($Z=0.0004$), which lead to better reproduce the observed β slope, but with metallicity values unrealistically low (e.g., ?). However, even this last set of assumptions does not yield satisfactory fits of the UV β slope for the most IR luminous galaxies: the β slopes predicted by the SED fits are redder than the observed ones.

Our study confirms previous results regarding ULIRGs

(e.g., Goldader et al. 2002; Reddy et al. 2010): ULIRGs generally have significantly redder IR/UV luminosity ratios that would be inferred from their UV slopes assuming the Meurer et al. (1999); Calzetti et al. (2000) attenuation curves.

Furthermore, depending on whether we assume energy balance, we have $\Delta \log f_{\text{EL}} = \log(f_{\text{EL}(\text{obs})}/f_{\text{EL}(\text{SED})})$ as high as ~ 1.0 dex. This is due to the large difference in dust attenuation derivation found for the ULIRGs between the two methods used here (with or without energy balance): the mean difference is $\Delta A_V = A_{V, \text{energy balance}} - A_{V, \text{no energy balance}} = 1.6$.

REFERENCES

- Adelberger, K. L., Steidel, C. C., Shapley, A. E., et al. 2004, *ApJ*, 607, 226, 226
- Akaike, H. 1974, *IEEE Transactions on Automatic Control*, 19, 716, 716
- Anders, P., & Fritze-v. Alvensleben, U. 2003, *A&A*, 401, 1063, 1063
- Bolzonella, M., Miralles, J., & Pelló, R. 2000, *A&A*, 363, 476, 476
- Bouché, N., Dekel, A., Genzel, R., et al. 2010, *ApJ*, 718, 1001, 1001
- Bouchet, P., Lequeux, J., Maurice, E., Prevot, L., & Prevot-Burnichon, M. L. 1985, *A&A*, 149, 330, 330
- Bruzual, G., & Charlot, S. 2003, *MNRAS*, 344, 1000, 1000
- Calzetti, D., Armus, L., Bohlin, R. C., et al. 2000, *ApJ*, 533, 682, 682
- Calzetti, D., Kinney, A. L., & Storchi-Bergmann, T. 1994, *ApJ*, 429, 582, 582
- Calzetti, D., Meurer, G. R., Bohlin, R. C., et al. 1997, *AJ*, 114, 1834, 1834

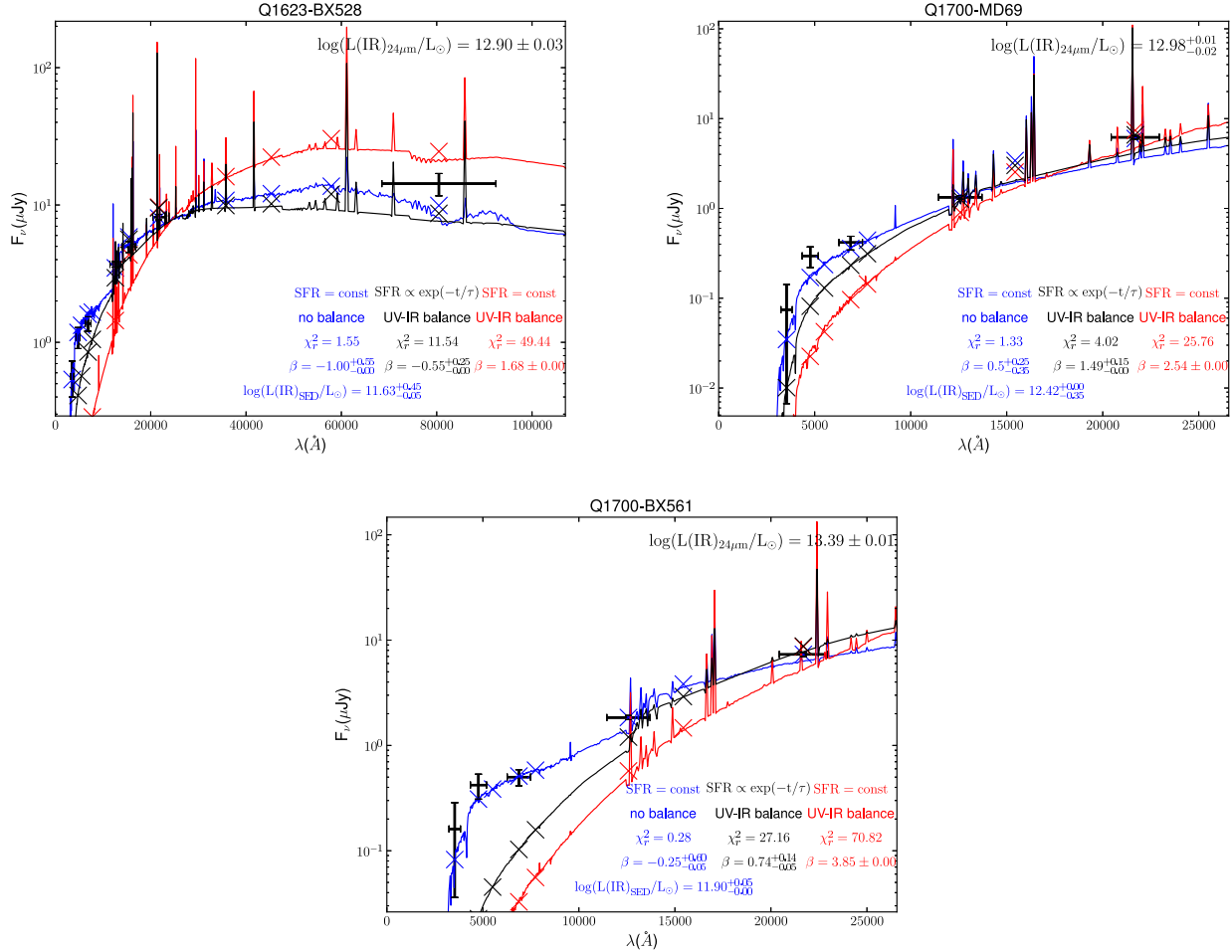


Figure 17. Continued.

Casey, C. M., Scoville, N. Z., Sanders, D. B., et al. 2014, *ApJ*, 796, 95, 95
 Castellano, M., Fontana, A., Grazian, A., et al. 2012, *A&A*, 540, A39, A39
 Chabrier, G. 2003, *PASP*, 115, 763, 763
 Charlot, S., & Longhetti, M. 2001, *MNRAS*, 323, 887, 887
 Chary, R., & Elbaz, D. 2001, *ApJ*, 556, 562, 562
 Chary, R.-R., Stern, D., & Eisenhardt, P. 2005, *ApJ*, 635, L5, L5
 Daddi, E., Dickinson, M., Morrison, G., et al. 2007, *ApJ*, 670, 156, 156
 Davé, R., Oppenheimer, B. D., & Finlator, K. 2011, *MNRAS*, 415, 11, 11
 de Barros, S., Schaerer, D., & Stark, D. P. 2014, *A&A*, 563, A81, A81
 Domínguez, A., Siana, B., Henry, A. L., et al. 2013, *ApJ*, 763, 145, 145
 Duncan, K., Conselice, C. J., Mortlock, A., et al. 2014, *MNRAS*, 444, 2960, 2960
 Erb, D. K., Steidel, C. C., Shapley, A. E., et al. 2006a, *ApJ*, 647, 128, 128
 —. 2006b, *ApJ*, 646, 107, 107
 Fioc, M., & Rocca-Volmerange, B. 1997, *A&A*, 326, 950, 950
 Förster Schreiber, N. M., Genzel, R., Bouché, N., et al. 2009, *ApJ*, 706, 1364, 1364
 Goldader, J. D., Meurer, G., Heckman, T. M., et al. 2002, *ApJ*, 568, 651, 651
 González, V., Labbé, I., Bouwens, R. J., et al. 2010, *ApJ*, 713, 115, 115
 Holden, B. P., Oesch, P. A., Gonzalez, V. G., et al. 2014, *ArXiv e-prints*, arXiv:1401.5490
 Kashino, D., Silverman, J. D., Rodighiero, G., et al. 2013, *ApJ*, 777, L8, L8
 Kennicutt, Jr., R. C. 1998, *ARA&A*, 36, 189, 189
 Kewley, L. J., Dopita, M. A., Leitherer, C., et al. 2013a, *ApJ*, 774, 100, 100
 Kewley, L. J., Maier, C., Yabe, K., et al. 2013b, *ApJ*, 774, L10, L10
 Kimura, M., Maihara, T., Iwamuro, F., et al. 2010, *PASJ*, 62, 1135, 1135
 Kriek, M., Shapley, A. E., Reddy, N. A., et al. 2015, *ApJS*, 218, 15, 15
 Krueger, H., Fritze-v. Alvensleben, U., & Loose, H.-H. 1995, *A&A*, 303, 41, 41
 Kulas, K. R., Shapley, A. E., Kollmeier, J. A., et al. 2012, *ApJ*, 745, 33, 33
 Kulas, K. R., McLean, I. S., Shapley, A. E., et al. 2013, *ApJ*, 774, 130, 130
 Labbé, I., González, V., Bouwens, R. J., et al. 2010, *ApJ*, 716, L103, L103

Labbé, I., Oesch, P. A., Bouwens, R. J., et al. 2013, *ApJ*, 777, L19, L19
 Law, D. R., Steidel, C. C., Shapley, A. E., et al. 2012, *ApJ*, 745, 85, 85
 Leitherer, C., & Heckman, T. M. 1995, *ApJS*, 96, 9, 9
 Madau, P. 1995, *ApJ*, 441, 18, 18
 Mancini, C., Förster Schreiber, N. M., Renzini, A., et al. 2011, *ApJ*, 743, 86, 86
 Marmol-Queraltó, E., McLure, R. J., Cullen, F., et al. 2015, *ArXiv e-prints*, arXiv:1511.01911
 McLean, I. S., Becklin, E. E., Bendiksen, O., et al. 1998, in *Society of Photo-Optical Instrumentation Engineers (SPIE) Conference Series*, Vol. 3354, *Infrared Astronomical Instrumentation*, ed. A. M. Fowler, 566–578
 McLean, I. S., Steidel, C. C., Epps, H. W., et al. 2012, in *Society of Photo-Optical Instrumentation Engineers (SPIE) Conference Series*, Vol. 8446, *Society of Photo-Optical Instrumentation Engineers (SPIE) Conference Series*
 Meurer, G. R., Heckman, T. M., & Calzetti, D. 1999, *ApJ*, 521, 64, 64
 Nakajima, K., & Ouchi, M. 2014, *MNRAS*, 442, 900, 900
 Nayyeri, H., Mobasher, B., Hemmati, S., et al. 2014, *ApJ*, 794, 68, 68
 Oesch, P. A., Labbé, I., Bouwens, R. J., et al. 2013a, *ApJ*, 772, 136, 136
 Oesch, P. A., Bouwens, R. J., Illingworth, G. D., et al. 2013b, *ApJ*, 773, 75, 75
 —. 2014, *ApJ*, 786, 108, 108
 Oke, J. B., & Gunn, J. E. 1983, *ApJ*, 266, 713, 713
 Oke, J. B., Cohen, J. G., Carr, M., et al. 1995, *PASP*, 107, 375, 375
 Ono, Y., Ouchi, M., Shimasaku, K., et al. 2010, *ApJ*, 724, 1524, 1524
 Ono, Y., Ouchi, M., Mobasher, B., et al. 2012, *ApJ*, 744, 83, 83
 Prevot, M. L., Lequeux, J., Prevot, L., Maurice, E., & Rocca-Volmerange, B. 1984, *A&A*, 132, 389, 389
 Price, S. H., Kriek, M., Brammer, G. B., et al. 2014, *ApJ*, 788, 86, 86
 Price, S. H., Kriek, M., Shapley, A. E., et al. 2015, *ArXiv e-prints*, arXiv:1511.03272
 Reddy, N., Dickinson, M., Elbaz, D., et al. 2012a, *ApJ*, 744, 154, 154

- Reddy, N. A., Erb, D. K., Pettini, M., Steidel, C. C., & Shapley, A. E. 2010, *ApJ*, 712, 1070, 1070
- Reddy, N. A., Pettini, M., Steidel, C. C., et al. 2012b, *ApJ*, 754, 25, 25
- Reddy, N. A., & Steidel, C. C. 2009, *ApJ*, 692, 778, 778
- Reddy, N. A., Steidel, C. C., Erb, D. K., Shapley, A. E., & Pettini, M. 2006a, *ApJ*, 653, 1004, 1004
- Reddy, N. A., Steidel, C. C., Fadda, D., et al. 2006b, *ApJ*, 644, 792, 792
- Reddy, N. A., Kriek, M., Shapley, A. E., et al. 2015, *ApJ*, 806, 259, 259
- Robertson, B. E., Ellis, R. S., Dunlop, J. S., McLure, R. J., & Stark, D. P. 2010, *Nature*, 468, 49, 49
- Robertson, B. E., Furlanetto, S. R., Schneider, E., et al. 2013, *ApJ*, 768, 71, 71
- Salmon, B., Papovich, C., Finkelstein, S. L., et al. 2015, *ApJ*, 799, 183, 183
- Salpeter, E. E. 1955, *ApJ*, 121, 161, 161
- Schaerer, D., & de Barros, S. 2009, *A&A*, 502, 423, 423
- . 2010, *A&A*, 515, A73+, A73+
- Schaerer, D., de Barros, S., & Sklias, P. 2013, *A&A*, 549, A4, A4
- Schaerer, D., & Pelló, R. 2005, *MNRAS*, 362, 1054, 1054
- Shapley, A. E., Steidel, C. C., Erb, D. K., et al. 2005, *ApJ*, 626, 698, 698
- Shapley, A. E., Reddy, N. A., Kriek, M., et al. 2015, *ApJ*, 801, 88, 88
- Shim, H., Chary, R.-R., Dickinson, M., et al. 2011, *ApJ*, 738, 69, 69
- Shivaei, I., Reddy, N. A., Steidel, C. C., & Shapley, A. E. 2015, *ApJ*, 804, 149, 149
- Siana, B., Teplitz, H. I., Chary, R.-R., Colbert, J., & Frayer, D. T. 2008, *ApJ*, 689, 59, 59
- Siana, B., Smail, I., Swinbank, A. M., et al. 2009, *ApJ*, 698, 1273, 1273
- Sklias, P., Zamojski, M., Schaerer, D., et al. 2014, *A&A*, 561, A149, A149
- Smit, R., Bouwens, R. J., Labbé, I., et al. 2014, *ApJ*, 784, 58, 58
- Smit, R., Bouwens, R. J., Franx, M., et al. 2015, *ApJ*, 801, 122, 122
- Stark, D. P., Ellis, R. S., Chiu, K., Ouchi, M., & Bunker, A. 2010, *MNRAS*, 408, 1628, 1628
- Stark, D. P., Schenker, M. A., Ellis, R., et al. 2013, *ApJ*, 763, 129, 129
- Steidel, C. C., Adelberger, K. L., Shapley, A. E., et al. 2003, *ApJ*, 592, 728, 728
- Steidel, C. C., Shapley, A. E., Pettini, M., et al. 2004, *ApJ*, 604, 534, 534
- Steidel, C. C., Rudie, G. C., Strom, A. L., et al. 2014, *ApJ*, 795, 165, 165
- Storey, P. J., & Hummer, D. G. 1995, *MNRAS*, 272, 41, 41
- Vanzella, E., Grazian, A., Hayes, M., et al. 2010, *A&A*, 513, A20, A20
- Vanzella, E., Fontana, A., Zitrin, A., et al. 2014, *ApJ*, 783, L12, L12
- Wild, V., Charlot, S., Brinchmann, J., et al. 2011, *MNRAS*, 417, 1760, 1760
- Wuyts, E., Rigby, J. R., Gladders, M. D., et al. 2012, *ApJ*, 745, 86, 86
- Wuyts, S., Förster Schreiber, N. M., Lutz, D., et al. 2011, *ApJ*, 738, 106, 106
- Yoshikawa, T., Akiyama, M., Kajisawa, M., et al. 2010, *ApJ*, 718, 112, 112
- Zackrisson, E., Bergvall, N., & Leitert, E. 2008, *ApJ*, 676, L9, L9